Physics-tailored machine learning reveals unexpected physics in dusty plasmas

Wentao Yu[a], Eslam Abdelaleem[a], Ilya Nemenman[a,b] (ID), and Justin C. Burton[a,1] (ID)

Dusty plasma is a mixture of ions, electrons, and macroscopic charged particles that is commonly found in space and planetary environments. The particles interact through Coulomb forces mediated by the surrounding plasma, and as a result, the effective forces between particles can be nonconservative and nonreciprocal. Machine learning (ML) models are a promising route to learn these complex forces, yet their structure should match the underlying physical constraints to provide useful insight. Here, we demonstrate and experimentally validate an ML approach that incorporates physical intuition to infer force laws in a laboratory dusty plasma. Trained on 3D particle trajectories, the model accounts for inherent symmetries, nonidentical particles, and learns the effective nonreciprocal forces between particles with exquisite accuracy ($R^2 > 0.99$). We validate the model by inferring particle masses in two independent yet consistent ways. The model's accuracy enables precise measurements of particle charge and screening length, identifying large deviations from common theoretical assumptions. Our ability to identify unknown physics from experimental data demonstrates how ML-powered approaches can guide new routes of scientific discovery in many-body systems. Furthermore, we anticipate our ML approach to be a starting point for inferring laws from dynamics in a wide range of many-body systems, from colloids to living organisms.

dusty plasma | machine learning | force inference

Dusty plasma is ubiquitous throughout the universe, from Saturn's rings to interstellar space (1–4), and is critically important for planet formation (5–7), technological processes (8–11), and potentially the emergence of life (12). In a dusty plasma, dust particles' interactions have known approximations based on tractable physics, yet they are poorly understood in environments that deviate from the simplest equilibrium conditions, for example, in systems with background plasma flows (13) or with external magnetic fields (14, 15). Particles interact through complicated forces mediated by the plasma environment (16), and violate some of our basic expectations: They are nonreciprocal and can source energy from their nonequilibrium environment (17–21). Limited information about these interactions can be obtained by carefully investigating quiescent systems of particles, for example, the Brownian motion of two particles (22–25) or the vibrational modes in a strongly coupled crystal (26–29). Yet particles must be highly dynamic and explore phase space to learn a separation-dependent interaction law (30, 31). Thus, compact and precise mathematical expressions that summarize interactions among dust particles as physical laws do not exist, yet some constraints on the interactions are clear. For example, the forces between particles are expected to be pairwise to leading order and to depend only on their mass, charge, and the spatial configuration (32–35). To handle this complexity, here we introduce a broadly applicable ML approach to infer new, previously unknown interactions in dusty plasmas. Our approach incorporates physical constraints in its underlying neural network architecture to learn the external forces and the unknown particle interactions directly from experimental data.

Broadly speaking, dusty plasma is a many-body system of interacting particles. Many-body systems are abundant in nature and continue to push the boundaries of science, from the detection of exoplanets (36, 37) to the behavior of living organisms (38–40). In these systems, interaction laws are often not well-defined, unlike Newton's laws of classical physics. However, the ability to generate large, precise datasets and the simultaneous emergence of machine learning (ML) to analyze them offer a path for inferring these interactions from experimental data. Many ML algorithms can model these complex systems by inferring parameters in a predefined mathematical description that best fit the data (41–45), or by finding a functional form describing the system within a constrained (though often large) library of possibilities (46–50). Other ML algorithms focus directly

Significance

Dusty plasma, a mixture of ions, electrons, and charged dust particles, is common throughout the universe. Understanding and modeling dusty plasma require precise knowledge of the complex interactions between dust particles, but machine learning (ML) is a promising approach for learning such interactions. In simulated data where the ground truth is known, ML models excel at making short-term predictions or inferring governing equations, yet there are few examples where new physical laws have been learned from real experimental data. Here, we demonstrate a scalable ML model that learns the complex interparticle forces from motion of particles in a laboratory dusty plasma. Our experiments and model reveal important discrepancies from common theoretical assumptions in dusty plasmas.

on predicting the future state of a system from its past without inferring or interpreting the underlying physics as an intermediate step (39, 42, 51–53). Often the data used to train and validate these models come from simulations with labeled ground-truth parameters, known particle properties, and provided, well-defined interaction laws. However, real experimental data lack all of these conveniences, and there have been recent attempts to extend ML methods to experimental data (39, 42, 50, 53–56). Nevertheless, endowing ML methods with constraints based on physical intuition can facilitate progress in realistic situations. This is especially important for many-body data, where such constraints are needed to tame the combinatorial complexity of interactions among the measured components (57), and as a result, physics-constrained machine learning for many-body systems is still emerging (41, 56, 58–69). Here, we simultaneously address many of these challenges by introducing a physics-constrained ML approach based on a neural network architecture that is designed to incorporate the physical intuition about the problem, and then use that architecture to approximate arbitrary forces between particles. This way we are able to learn *new*, unanticipated interaction laws from dusty plasma experiments.

In a dusty plasma, the equilibrium charge, $-q$, on a given particle is determined by a balance of ion and electron currents to the surface, and the currents are determined by the local plasma environment (ion and electron densities and velocity distributions). Usually particles acquire a negative charge, and thus repel. However, the interaction force is screened by the plasma environment, and the screening length λ is of fundamental importance since it determines the effective range of interaction. Moreover, when particles are levitated in a plasma sheath near a conducting wall (electrode with negative charge, Fig. 1 *A–C*), q will be a function of the particle's vertical z position within the plasma sheath. The particles are also immersed in a fast-flowing "river" of positive ions that are attracted to the electrode and move at speeds in excess of 2 km/s (Bohm velocity). The deflection of these ions in the negative z-direction produces an ion wake beneath each particle (71, 72), and the effective interactions between particles include this ion wake (Fig. 1*C*). The wake-mediated interaction is nonreciprocal, breaks translational symmetry in z, and is predicted to cause attractive forces when particles are close. Since dusty plasmas are readily confined and manipulated in the laboratory, they offer an ideal platform to study complex and emergent collective behavior in particulate matter.

To infer interaction laws in dusty plasma, we captured three-dimensional (3D) trajectories of individual dust particles using scanning laser sheet tomography (70). Our physics-constrained neural network model used these trajectories to infer nonreciprocal interactions between individual pairs of nonidentical particles, environmental forces that trap particles and drive their motion, and velocity-dependent drag forces from the background gas. The inference procedure compared the sum of these forces to the experimental acceleration of each particle. Remarkably, the model was extraordinarily accurate when fitting the acceleration,
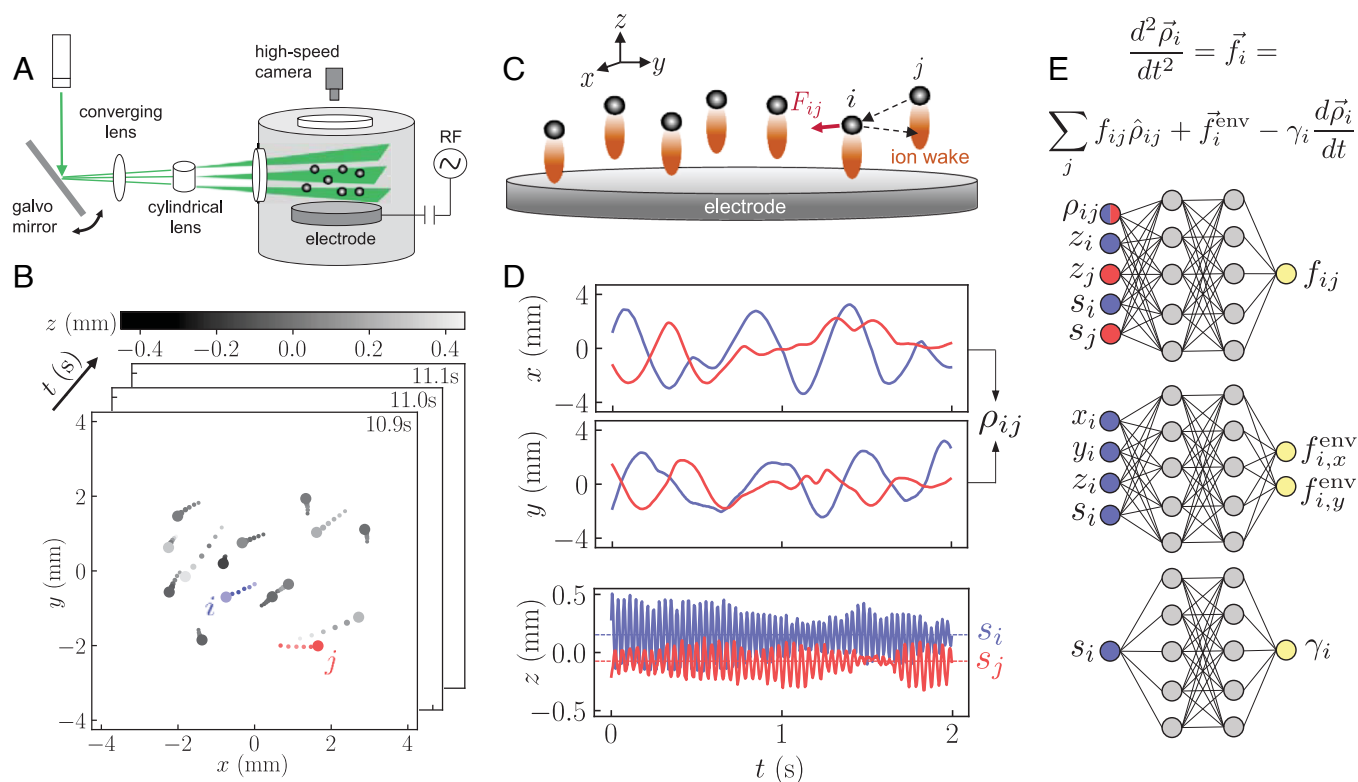

Fig. 1. Overview of experiment and data workflow. (*A*) Charged microparticles are levitated in an RF-driven plasma sheath above a flat electrode. Their motion is imaged using a scanning laser sheet coupled to a high-speed camera (70). (*B*) Snapshot of particle positions from a single experiment of 15 particles. The grayscale color indicates the z-position, and the tails of each particle represent the previous five frames. (*C*) The focused ion wake (red) is directly below each particle, and contributes a small attractive part of the total force (F_{ij}) on particle i, so that the overall interaction is nonreciprocal. (*D*) The x, y, and z position of two particles during two seconds. The particles are marked i (blue) and j (red) in panel (*C*). The quantity $s_i = \langle z_i \rangle$ depends on the particle size and mass and hence is used as a descriptor for each particle. (*E*) The objective is to infer the horizontal reduced forces on particles using Newton's equation of motion. The schematic of the model, which consists of three neural networks trained concurrently and act as nonlinear approximators to the three terms in the equation (particle interactions—f_{ij}, environmental forces—$\vec{f}_{env}$, and damping from the background gas—γ_i). The input color designates the source (particle i or j).

achieving $R^2 > 0.99$ over multiple experiments. To verify that the model learned each force accurately, we compared the mass, m, of each particle in two independent ways, which agreed with each other (and the known size of the particles using optical microscopy). For particles in the same horizontal plane, we fitted the interaction force of each particle pair to a well-known analytical approximation (16, 30), allowing us to simultaneously extract m, q, and λ. Contrary to conventional assumptions where λ depends solely on plasma properties, we find that the fitted value of λ increases with the average size of interacting particles. Furthermore, we find that $q \sim m^p$, where p ranges between 0.30 and 0.80 and increases with background gas pressure. This variation contrasts with the simplest assumptions of particle charging in dusty plasmas where $q \propto m^{1/3}$ (2, 73).

Experiments and Model

Our dusty plasma experiments utilized a vacuum chamber filled with argon gas at 0.5 to 1.5 Pa of pressure (Fig. 1A)—a setup similar to our previous experiments (25, 31, 70, 74). A disk-shaped electrode was driven with RF power and generated a weakly ionized argon plasma. Near the electrode surface, micron-sized charged particles were levitated in a plasma sheath—a sharp gradient in the electric field where electrostatic forces can balance with gravitational forces (75). The levitated particles explored a space roughly 10 mm × 10 mm × 1 mm in size (Fig. 1B and Movie S1). The particle positions were tracked using 3D scanning laser tomography (70). For more details about the plasma conditions and particle tracking method, see *Materials and Methods*.

The interaction between each pair of particles is mostly due to electrostatic repulsion since each particle carries a negative charge ($\approx 10^4 e$). However, in the plasma sheath, ions stream past each particle at speeds greater than 2 km/s, resulting in vertical ion wakes (Fig. 1C), similar to the wakes produced behind a fast-moving boat in open water. The wakes make the overall interactions between particles nonreciprocal, i.e., $\vec{F}_{ij} \neq -\vec{F}_{ji}$ (17–21), and they are especially important when particles are vertically separated in the z direction. Moreover, since the particle charge varies within the plasma sheath, the particle interactions break translational symmetry in z, while maintaining translational symmetry in the xy-plane. To learn these complex forces, we overcome a major challenge: building the required physical symmetries into a model that can be trained on systems with varying particle number.

The tracked 3D trajectories $(x_i(t), y_i(t), z_i(t))$ of all the particles were used as input to train our ML model. An example of trajectories for two particles is shown in Fig. 1D. The model assumes that the horizontal (xy-plane) acceleration of each particle is determined by Newton's second law:

$$\ddot{\vec{\rho}}_i = \vec{f}_i = \sum_{j \neq i} f_{ij}\hat{\rho}_{ij} + \vec{f}_i^{\,\text{env}} - \gamma_i\dot{\vec{\rho}}_i, \qquad [1]$$

where $\vec{f}_i$ is the horizontal reduced force on particle i, or equivalently the net force, $\vec{F}_i = (F_{i,x}, F_{i,y})$, divided by its mass, m_i. Dotted variables represent differentiation with respect to time. The position and displacement vectors are $\vec{\rho}_i = (x_i, y_i)$ and $\vec{\rho}_{ij} = (x_i - x_j, y_i - y_j) = \rho_{ij}\hat{\rho}_{ij}$, where $\hat{\rho}_{ij}$ is the direction of the reduced horizontal interaction force from particle j to i, and $f_{ij} = F_{ij}/m_i$, where F_{ij} is the magnitude of the force. Since the ion wake is directly below each particle, as shown in Fig. 1C, the ion wake will change the direction of the z-component of the

force, but interaction forces in the xy-plane will still point along $\hat{\rho}_{ij}$ (21). The reduced environmental force is $\vec{f}_i^{\,\text{env}} = \vec{F}_i^{\,\text{env}}/m_i$, where $\vec{F}_i^{\,\text{env}}$ is the horizontal environmental force on particle i, and the damping coefficient of particle i is γ_i. Particles are strongly confined by gravity and electrostatic forces in the z-direction, which are about 100 fold larger than other forces in the system, as evidenced by the different frequencies and amplitudes of motion shown in Fig. 1D.

Although we can accurately track the z position of each particle since the vertical oscillation frequency was ≈ 25 Hz (Fig. 1D) and our sampling rate was 200 Hz, inferring forces in our model requires integrating the data over a small time window (*SI Appendix*, Eq. S5), which would necessitate a higher time resolution for z force inference. Thus, in this study, we only aim to infer forces in the xy-plane, which will generally depend on the z position of each particle. Importantly, the particles in our experiments were not identical and the model requires particle-level descriptors. Ideally, this would be the mass of each particle, which is unknown. But in our experiments, heavier particles sat lower in the plasma sheath so that their averaged z position over the entire time series acted as a good proxy for the particle mass. Thus we defined $s_i = \langle z_i \rangle_t$ as a "descriptor" that monotonically decreased with the particle size, even though the exact quantitative dependence is unknown.

In the model, three neural networks (NNs) act as universal approximators to the three types of forces on each particle (Fig. 1E). We use three independent networks because they represent different terms in the equation of motion of a single particle, Eq. 1. Each network must necessarily have different inputs, otherwise we would not be able to distinguish the learned forces from the three terms. We denote a NN as g or $\vec{g}$ (a function whose output is a scalar or vector), to avoid ambiguity with outputs such as f or $\vec{f}$ (scalar or vector). The first NN, g_{int}, requires ρ_{ij}, z_i, z_j, s_i, and s_j as inputs. It outputs the magnitude of the effective reduced interaction force, f_{ij}. We note that this structure conserves translational symmetry in x and y, but breaks this symmetry in z. The second NN, $\vec{g}_{\text{env}}$, requires x_i, y_i, z_i, s_i as inputs. It outputs both components of the vector, $\vec{f}_i^{\,\text{env}}$. The third NN, g_γ, uses s_i as its sole input, and outputs the drag coefficient, γ_i. Requiring a drag force linear in velocity is supported by theory: According to Epstein's law (76), for spherical particles with a density of 1,510 kg·m^{-3} inside argon gas (16),

$$\gamma_i = \frac{12.2P}{d_i}\,\mu\text{m} \cdot \text{Pa}^{-1} \cdot \text{s}^{-1}. \qquad [2]$$

Here, P is the plasma pressure and d_i is the diameter of particle i. Inferring an individual particle's damping coefficient provides direct information about its size (and mass), thus g_γ constructs a map from the size descriptor s_i to the physical parameter γ_i (or m_i).

During training, the model adjusts the weights in each neural network concurrently to minimize a loss function that compares the predicted reduced force, $\vec{f}_i$, to the measured horizontal acceleration, $\ddot{\vec{\rho}}_i$. Since we are calculating the forces between all pairs of particles, the total training time scales as N_p^2, where N_p is the number of particles. To reduce noise, we use the weak form of our loss function (77), a technique that calculates a filtered version of acceleration from experimental data by integrating trajectories over a small time window instead of computing derivatives from the noisy position time series (i.e., *SI Appendix*, Eq. S5). As a simple example, consider the function centered at $t = 0$:

Table 1. Parameters and model performance from five experiments

N_p	P (Pa)	z_{std} (mm)	ρ_{std} (mm)	Test R^2	Color
9	1.00	0.060	0.96	0.9949	Blue
10	1.00	0.10	1.23	0.9921	Green
13	1.00	0.082	1.14	0.9912	Red
15	0.75	0.12	2.24	0.9919	Orange
18	1.20	0.033	1.38	0.9963	Purple

N_p is the number of particles, P is the neutral gas pressure, z_{std} and ρ_{std} are the SD of the particle motion in the vertical and horizontal directions, respectively, and are averaged over all particles. Test R^2 is the R^2 score of the model performance on the test dataset. Each experiment is assigned a color, indicated by the last column, which is plotted in Fig. 4.

$w(t) = (1 - t^2)^2$. Since $w(\pm 1) = 0$ and $\dot{w}(\pm 1) = 0$, it is straightforward to show using integration by parts that:

$$\int_{-1}^{1} \ddot{x} w \, dt = \int_{-1}^{1} x \ddot{w} \, dt. \qquad [3]$$

This replaces a noisy second derivative of an experimental time series with exact derivatives of an analytic function (w). We found that this dramatically increased the model performance (R^2) and was a necessary part of our methodology. We also use the Huber loss to reduce the influence of outliers in the data, which occur when two particles are closely separated and experience large accelerations that can be hard to resolve. The complete details of the model structure, the full equation of the loss function and its minimization, and the application of the weak form are described in *SI Appendix*.

Results and Discussion

The presentation of our results is organized as follows. We first demonstrate the model's accuracy in predicting experimental trajectories using the sum of the three force components in Eq. **1**. Next we show that model's prediction on position-dependent interaction and environmental forces (the first two terms on the right-hand side of Eq. **1**). We then subsequently fit the predicted interaction (reduced force) using a well-known theory to extract estimates of each particle's charge, mass, and pairwise screening length. Finally, we verify the mass estimate by directly comparing it with expectations from the damping coefficient (last term in Eq. **1**) and discuss deviations of the fitted charge and screening length from conventional plasma physics theory.

Model Accuracy in Fitting Acceleration. We used the model to infer forces on particles from five experiments (Movies S1–S5) carried out under different conditions: number of particles, gas pressure, and plasma conditions. At least ∼9 particles were necessary to produce a highly dynamic system; smaller systems with less particles tended to form rotating crystalline structures (Movies S6 and S7). We performed 10-fold cross-validation on each experiment. That is, the data, ordered by time, was split into 10 equal parts. We created 10 independent models where the k-th model ($k = 1, 2, \ldots, 10$) used the k-th part as the validation set while the other nine parts were used for training. The model's performance was evaluated by computing the R^2 score on the validation set. The errors presented in our results represent the SD of the prediction from all 10 models. Further details can be found in *SI Appendix*.

For each experiment, the average R^2 of the 10 models was always larger than 0.99 (Table 1). For visual reference of the

model performance, we show data for the x and y acceleration on two different particles and the corresponding model prediction in Fig. 2 *A* and *B*. This remarkable agreement is representative of all 49.4 s of data captured in the experiment. We note that a high R^2 only indicates that the model fits the *sum* of the three reduced force components in Eq. **1**, and does not necessarily indicate that *each* component is fit correctly. Thus, we ensured that the set of input parameters for each component was parsimonious and reflected the symmetries in our experiment, i.e., $x_i - x_j$ and $y_i - y_j$ only appear in the particle separation, ρ_{ij}, used as an input to g_{int}, while z_i and z_j appear as direct inputs to g_{int}. Furthermore, as we will show, the accuracy of each component is validated by inferring particle-level properties in two independent ways.

Model Prediction for Each Force Component. Recent studies have demonstrated that effective interaction forces can be learned from data by assuming all particles are identical, for example, by using Underdamped Langevin inference on stochastically driven systems (49), or by representing the particle interactions using graph neural networks (GNNs) (56). GNNs can also learn interactions between nonidentical particles experiencing pairwise, reciprocal interactions (50, 78). Our model for particle interactions can be viewed as a single-iteration GNN, in which the total interaction on a particle is the linear sum of the interactions of all other particles, because in dusty plasma, the interaction is pairwise to leading order. Yet in contrast to these examples, our model predicts the effective reduced interaction force, f_{ij}, which can be nonreciprocal, between *any* particle pair i and j at *any* position represented in the experimental data. Moreover, the model simultaneously and independently learns environmental forces and velocity-dependent drag forces on individual particles.

For simplicity, since $\rho_{ij} = \rho_{ji}$, we use ρ to denote the horizontal separation of two particles. Fig. 3*A* demonstrates the model's ability to capture nonreciprocal interactions for two nearly identical particles with descriptors $s_1 \approx s_2$ at different vertical positions, $z_1 < z_2$. Nonreciprocity is clearly observed
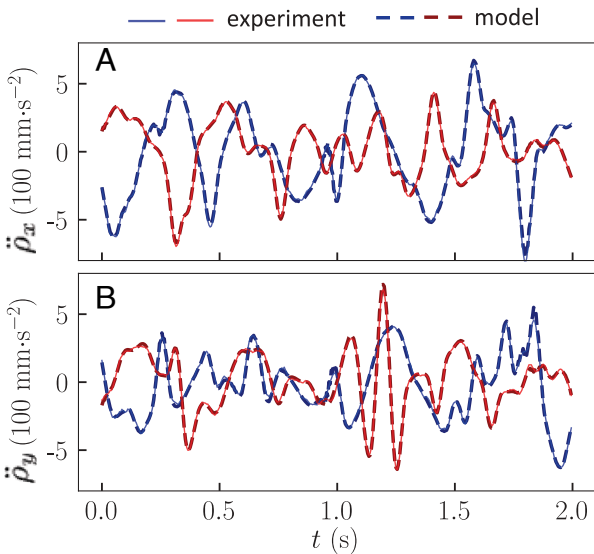

Fig. 2. The predicted reduced force ($\bar{f}$, dashed lines) and measured experimental acceleration ($\ddot{\rho}$, solid lines) for two particles (red and blue) in the 15 particle system. We note that this is *test data*, meaning it was not used to train the model. Data are shown for 2 s out of the 4.94 s of test data. The entire experiment was 49.4 s long. (*A*) f_x and $\ddot{\rho}_x$ and (*B*) f_y and $\ddot{\rho}_y$. The two particles are the same particles shown in Fig. 1*D*.

for $\rho < 0.6$ mm, and $f_{21}/f_{12} \approx 2$ at the shortest separation. For the same particles with a larger vertical separation, f_{12} is attractive (Fig. 3 *A, Inset*). The dramatic nonreciprocity is due to the presence of the ion wake structure beneath each particle, as shown in Fig. 1*C* (79). However, interactions are expected to be reciprocal when $z_i = z_j$ (21). This reciprocity is illustrated in Fig. 3*B* for the same two particles (the main panel) and two different particles (*Inset*).

In this reciprocal regime, we used the well-known screened Coulomb interaction to fit the prediction of the model:

$$m_i f_{ij} = m_j f_{ji} = \frac{A}{\rho}\left(\frac{1}{\rho} + \frac{1}{\lambda}\right)e^{-\rho/\lambda}. \qquad [4]$$

Here, the coefficient A is a fitting parameter, but theory suggests that $A = q_i q_j / 4\pi\epsilon_0$, where q_k and m_k are the charge and mass of particle k, respectively, ϵ_0 is the permittivity of free space, and λ is the effective screening length (2, 16, 30). Importantly, systematic error can be clearly observed in the fit (solid lines in Fig. 3*B*), indicating that there are deviations from Eq. **4** as a universal law for all particle separations. This deviation is expected since the real interaction involves both negatively charged particles and their associated ion wake structures. These structures are often modeled as a virtual, positive charge below each particle (80). Nevertheless, Eq. **4** is a good analytical approximation for each pair of particles when they are at the same z, although as we will show, care must be taken when interpreting both q and λ from the fits to Eq. **4**. When $z_i = z_j$, but $s_i \neq s_j$, as shown in the *Inset* of Fig. 3*B* for different particles with indices 1 and 3, the reduced force can be shifted to coincide using a multiplicative factor of 2.6. This factor is the particles' mass ratio, m_3/m_1, when the forces are reciprocal ($F_{13} = F_{31}$).

In addition to the dependence on ρ, the model can predict the dependence of the interaction force on z, revealing the spatial structure of the plasma sheath. Fig. 3*C* shows the reciprocal reduced force versus z for particles 1 and 2 when $z_1 = z_2 = z$. At larger z, the force is nearly uniform, but then rises precipitously as z decreases, more than a factor of two over a span of 200 µm. This sharp rise is mostly due to the variation of accumulated charge on each particle. In the bulk plasma, properties such as the ion and electron temperature and density are expected to be constant (81, 82). Thus, the particle charge should also be constant. However, inside the plasma sheath, these properties change, and the charge on the particles can increase dramatically (74, 83). This is also evidenced by an increase of the screening length (λ) at the boundary of the plasma sheath (*SI Appendix, Fig. S1*). Additionally, we show the model's prediction of the reduced environmental force ($\vec{f}_i^{\text{env}}$) in Fig. 3*D*. This force acts on each particle separately and is due to local electric fields and ion drag forces that trap the particle and drive its vortical motion, resulting in trajectories in the xy-plane that resemble Fig. 1*D*. Taken together, Fig. 3 shows how our ML model can turn the particles into nonintrusive, local probes of the plasma environment.

Estimating Particle Mass, Charge, and Interaction Range. In many-body systems, measured properties of individual particles are often inaccessible or assumed from simple theories, yet our ML approach can infer both the mass and charge of each particle from experimental data alone. Our approach is similar to a recent two-step method that infers the force, and then infers particle properties (i.e., mass) from an analytic expression (50, 78). Using nonlinear regression (*Materials and Methods*), we simultaneously
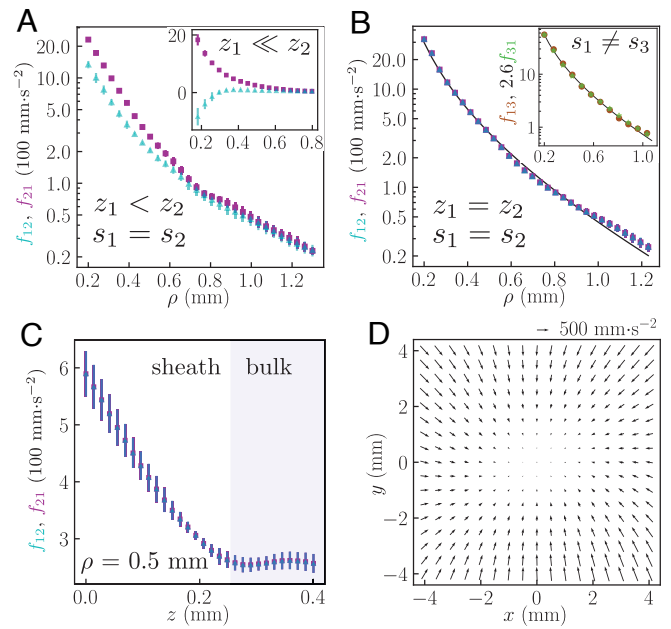

Fig. 3. Model prediction of interaction and environmental reduced forces for the 15-particle experiment. (*A*) The magnitude of the reduced interaction force (f_{12}, cyan triangles; f_{21}, purple squares) between two similar particles ($s_1 = 0.234$ mm, $s_2 = 0.232$ mm), at $z_1 = 0.15$ mm and $z_2 = 0.30$ mm. The force is plotted versus the horizontal separation ρ. The *Inset* shows the interaction at $z_1 = 0.05$ mm and $z_2 = 0.35$ mm. (*B*) The model predicts the same two particles' interaction is reciprocal at $z_1 = z_2 = 0.15$ mm. The black solid line is a fit of the average of the two predictions to Eq. **4** with $\lambda = 0.42$ mm. The *Inset* shows the interaction of two different particles (f_{13}, brown circles; f_{31}, green stars) at $z_1 = z_3 = 0.15$ mm. Here, $s_3 = -0.053$ mm, and f_{31} is shifted by a factor of 2.6 (the mass ratio) to collapse the curves. The black solid line is a fit to Eq. **4** with $\lambda = 0.48$ mm. (*C*) f_{12} and f_{21} evaluated at $\rho = 0.5$, plotted versus $z = z_1 = z_2$. The sharp rise in the model prediction indicates the boundary between the plasma sheath and bulk plasma (purple). (*D*) Environmental reduced force field of particle 1, $\vec{f}_1^{\text{env}}$, at $z_1 = 0.15$ mm. The error bars represent the SD of the prediction from 10 models trained on different sections of the experimental data, as detailed in *SI Appendix*.

fitted the model's predicted interaction (e.g., Fig. 3*B*) to Eq. **4** for every pair of particles in each experiment at $z = 0.03$ mm, with fitting parameters m_i, q_i, q_j, and λ_{ij}. To obtain good fits, it was necessary to allow the screening length (λ_{ij}) to vary between particle pairs, rather than be represented by a single constant that only depends on the plasma environment. This is evidenced in Fig. 4*A*, where f_{ij} is plotted for a pair of small particles, and a pair of large particles. The screening length varies by almost a factor of 3.

In the plasma sheath where particles are levitated, the supersonic motion of ions toward the electrode (negative z-direction) diminishes their ability to screen the charged particles (72, 84), meaning that, to the lowest order, λ should be determined by the electron screening length [1 to 2 mm in our experiments (74)]. However, the effective interactions between particles involve their associated ion wakes; the same wakes that give rise to nonreciprocal interactions (Fig. 1*C*). As the particle separation $\rho \to 0$, particles repel strongly through a Coulomb force representing the *actual* charge on each particle. For large ρ, the effective particle charge is reduced by the virtual positive charge (ion wake). Thus, fitting the total interaction with Eq. **4** should result in λ being significantly less than the plasma Debye length. Also, λ should depend on the strength and spatial extent of each particle's ion wake, which can lead to an apparent dependence on particle size. Indeed, an increase of λ with particle size has been reported in experiments examining the linearized
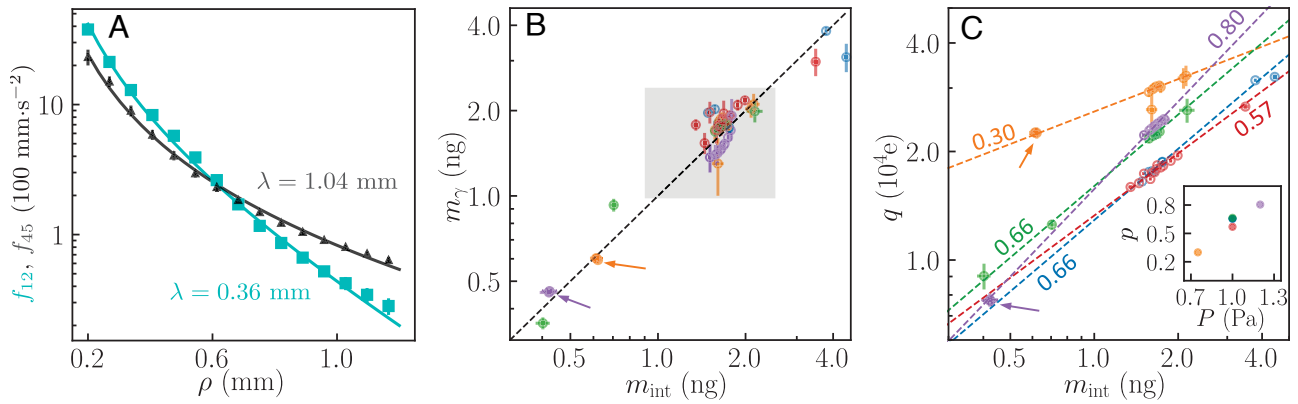
Fig. 4. The inferred measurements of mass, charge, and screening length using Eq. **4**, at $z = 0.03$ mm. (*A*) In the 15-particle experiment, the interaction between small particles 1 and 2 ($s_1 = 0.234$ mm, $s_2 = 0.232$ mm, cyan) and between large particles 4 and 5 ($s_4 = -0.150$ mm, $s_5 = -0.161$ mm, gray) have a distinctly different decay with length scale λ. The solid lines are fits using Eq. **4**. Note that a larger λ means slower decay. (*B*) The mass of all particles inferred from the drag coefficient (m_γ) versus the mass inferred from the particle interaction (m_{int}). Different colors represent the five different experiments (Table 1). The dashed line is the theoretical value of $m_\gamma = m_{\text{int}}$. The gray box represents particles with an average diameter of 12.8 ± 0.32 μm, corresponding to a mass of $m_0 = 1.65 \pm 0.12$ ng, which is necessary for quantifying the mass (see *SI Appendix* for more information). (*C*) Particles charge, q, versus m_{int}, both inferred from the fitting procedure using Eq. **4**. The dashed lines are power law fits with the fitting power p displayed alongside the lines. In both panels, the two clusters of purple and orange data (indicated by the arrows) each consist of five similar particles whose manufacturer-labeled diameters are 9.46 ± 0.10 μm (0.66 ± 0.02 ng) and 8.00 ± 0.09 μm (0.40 ± 0.01 ng), respectively. *Inset*: The fitting power p versus the plasma pressure P. Note that the blue and green data coincide.

vibrational motion of dust particles (85), and our results firmly demonstrate that Eq. **4** is an approximation whose parameters must be carefully interpreted when considering effective particle interactions in dusty plasmas.

In addition to λ, our fitting procedure provides the mass and charge of each particle from the interaction. To validate this procedure, we obtained an independent estimate of the mass from the inferred damping coefficient (γ) by computing the particle's diameter using Eq. **2** and assuming the particles were spheres with density 1,510 kg·m^{-3}. These two independent masses, denoted $m_{i,\text{int}}$ and $m_{i,\gamma}$, show excellent agreement (Fig. 4*B*), demonstrating that the model correctly infers each term in Eq. **1** using experimental data. However, the inference of the particle charge (q_i) from Eq. **4** reveals important discrepancies from widely used theoretical assumptions. Orbital-motion-limited (OML) theory predicts the charge on a spherical particle in a dusty plasma under the assumption the electron and ion temperatures (and densities) are known and uniform, and collisions are ignored (2, 86–88). Under these assumptions, two particles of different sizes *should* act as spherical capacitors and have the same floating potential, $V_i = 2\pi\epsilon_0 d_i q_i$. Thus, we expect $q_i \propto m_i^{1/3}$ since $m_i \propto d_i^3$. We tested this relationship by fitting the inferred charge versus mass in all five experiments using $q_i \propto m_i^p$. As shown in Fig. 4*C*, the power p ranged from 0.30 to 0.80, and increased monotonically with pressure P (Fig. 4 *C*, *Inset*). Thus, even when the particle charge is inferred at the same z-position, where plasma properties should be the same for all particles, the power p can vary substantially from the expected value of 1/3.

The validation of the particle mass (Fig. 4*B*) suggests that the prefactor A in Eq. **4** is estimated correctly, and thus so is the particle charge. While it is possible that the presence of a positive ion wake reduces the effective charge of each particle at large ρ, this effect would be negligible as $\rho \to 0$, where the quality of the fits to the interaction force are equally good. Given the pressure dependence observed in the *Inset* of Fig. 4*C*, it is natural to ascribe this variation in p to collisions between ions and neutral atoms, which are often ignored in theories of particle charging, yet collisions should reduce the charge of larger particles due to their increased capture radius (89, 90),

thereby making $p < 1/3$. As such, the origin of this discrepancy from common theoretical assumptions remains unclear, but our results highlight the need for more comprehensive theories of particle charging in plasma sheaths. Last, to ensure that our measurements of the screening length and particle charge are not artifacts of the inference process and accurately represent the physics, we simulated systems of many particles with similar nonreciprocal forces and environmental forces as in the experiment, and required that $q_i \propto m_i^{1/3}$ and a screening length independent of particle size (see the full details in *SI Appendix* and Movie S8). The model achieved a validation $R^2 = 0.9989$ and showed a 35% reduction of the inferred screening length in the presence of virtual positive charges representing the ion wakes beneath each particle (*SI Appendix*, Fig. S2*A*). Importantly, the model performed remarkably when extracting the reduced mass and charge of each particle (*SI Appendix*, Fig. S2 *B* and *C*), demonstrating that the inferred deviations from $q \propto m^{1/3}$ in experimental data are likely real.

Summary and Conclusions

We have developed a machine learning model that accurately infers the forces acting on individual particles in a many-body system. What makes this model different from past approaches is its ability to approximate complex, nonlinear interaction laws using NNs, treat particles as different individuals, build in physical symmetries into the model structure, and to learn purely from experimental data. By applying this approach to dusty plasmas, we learned both environmental forces and pairwise interaction forces between particles, and extracted the mass and charge of each particle in situ. In doing so, we verified theoretical predictions of nonreciprocal and attractive forces between dust particles, identified an unexpected dependence of the screening length on the size of interacting particles, and identified unexpected deviations from OML theory (where $q \propto m^{1/3}$).

Furthermore, we highlight that the primary challenge in uncovering the dependence of λ and q on particle size lies in controlling the variable z, since λ and q steeply vary with

the depth in the plasma sheath (z-direction). In equilibrium, heavier particles settle at lower z, rendering normal mode analysis approaches near the particles' equilibrium positions ineffective for comparing particles with different sizes (22, 24–29). Therefore, we expect these results to serve as seeds for new directions of research in dusty plasma physics.

Outside of dusty plasma research, our ML approach is widely applicable to physical and biological systems composed of many interacting agents. They can be active or passive, with arbitrarily complex interactions. Although intuition guides the underlying symmetries and expected structure of the model, the ability to surpass intuition and avoid biased assumptions is an essential first step in discovering new scientific laws from experiments.

Materials and Methods

Dusty Plasma Experiments. In our experimental vacuum chamber, a disk-shaped aluminum electrode with a 15 cm diameter was driven with 13.56 MHz RF power (2 to 7 W) to generate a weakly ionized plasma. The ion and electron density was ≈ 2 to 6×10^{13} m^{-3}, as measured with a custom Langmuir probe (74). Since the electron temperature (1 to 2 eV) was much higher than the ion and neutral gas temperature (0.04 eV), the electrode developed a negative bias voltage (-15 to -5 V). Particles were introduced into the plasma by mechanical agitation of a reservoir and developed a negative bias voltage as well, leading to an electrostatic repulsion from the electrode that levitated them ≈ 4.2 mm above the electrode surface. Most experiments confined 10 to 20 spherical melamine-formaldehyde (MF) particles (microParticles GMBH) in the plasma, and we purposefully used a combination of manufactured particles with labeled diameters of 12.8 ± 0.32 μm, 9.46 ± 0.10 μm, and 8.00 ± 0.09 μm since our model is able to handle different particle sizes. A unique feature of our experiments was a cylindrical neodymium magnet with diameter 7.5 cm placed inside the electrode, resulting in a nonuniform magnetic field of strength ≈ 0.04 T where the particles levitated. The gradient in the field produced a vortical ion flow and ion drag force on each particle, resulting in a highly dynamic system of particles with circulation.

3D Particle Tracking Method. To track the position of each particle, we used a rapidly scanning laser sheet synchronized to a high-speed camera, as shown in Fig. 1A. The laser scanning frequency was 200 Hz with a peak-to-peak amplitude of ≈ 4 mm at the position of the particles. The high speed camera was set to record at 8,000 fps, thus we obtained ≈ 40 images in one vertical sweep of the laser sheet. The resulting images were analyzed by TrackPy (91), and special care was taken to distinguish particles with very small separations. The ultimate spatial resolution of the in-plane x and y positions was 50 μm per pixel, and the

vertical z resolution was 100 μm per pixel. The tracking error is about 0.1 pixel. More complete details of the 3D tracking method can be found in refs. 25 and 70.

Fitting of Charge and Mass for Each Particle. For extracting m_i and q_i, we used a screened Coulomb interaction f^C:

$$f^C(\rho; q_i, q_j, m_i, \lambda_i, \lambda_j) = \frac{q_i q_j}{4\pi \epsilon_0 m_i \rho} \left(\frac{1}{\rho} + \frac{1}{\sqrt{\lambda_i \lambda_j}} \right) e^{-\rho/\sqrt{\lambda_i \lambda_j}}. \quad [5]$$

In order to find the mass and charge of all particles at a specific z position, we performed a global least-squares fit of every pair of particle interactions. For example, for a given z position, let $\bar{f}_{ij}(\rho)$ represent the model's prediction of particle j's reduced force on i at vertical position $z_i = z_j = z$ and horizontal separation ρ:

$$\bar{f}_{ij}(\rho) = \frac{g_{\text{int}}(\rho, z, z, s_i, s_j)}{\rho}. \quad [6]$$

In the fitting procedure, we aim at finding the optimal values of $\{q_i, q_j, m_i, \lambda_i, \lambda_j\}$ that minimize the following loss function:

$$L^C = \sum_{i=0}^{N_p} \sum_{j=0, j\neq i}^{N_p} \sum_{\rho}^{[a,b,c]} \left(\bar{f}_{ij}(\rho) - f^C(\rho; q_i, q_j, m_i, \lambda_i, \lambda_j) \right)^2. \quad [7]$$

Here, $[a, b, c]$ defines which particle interactions to include in the sum. The minimum separation is $\rho = a$, the maximum separation is $\rho = b$, and particles within a small range c are included at each separation. For Fig. 3, we chose $a = 0.3$ mm, $b = 1.2$ mm, and $c = 0.01$ mm. We note that the charge and the mass are coupled in the fitting procedure since they appear as a ratio. For example, if we decrease all particles' mass by a factor of 4, and decrease all particle's charges by a factor of 2, the fitting quality would not change. Thus, we added a constraint in the fitting that the average mass of the particles in the shaded area in Fig. 4B should be 1.65 ng, the average mass reported by the manufacturer. The above procedure was implemented for each of the 10 trained models, and the average q_i and m_i over all 10 models plus their SD is reported in Fig. 4.

Data, Materials, and Software Availability. Experimental data and machine learning code data have been deposited in https://github.com/wyu54/many-body-force-infer (92).

1. R. Merlino, Dusty plasmas: From Saturn's rings to semiconductor processing devices. *Adv. Phys. X* **6**, 1873859 (2021).
2. A. Melzer *et al.*, *Physics of Dusty Plasmas* (Springer, 2019), vol. 962.
3. R. Hippler, H. Kersten, M. Schmidt, K. H. Schoenbach, *Low Temperature Plasmas*, R. Hippler *et al.*, Eds. (Berlin: Wiley, 2008), vol. 787.
4. M. Chaudhuri, A. V. Ivlev, S. A. Khrapak, H. M. Thomas, G. E. Morfill, Complex plasma-the plasma state of soft matter. *Soft Matter* **7**, 1287–1298 (2011).
5. C. Goertz, Dusty plasmas in the solar system. *Rev. Geophys.* **27**, 271–292 (1989).
6. J. E. Wahlund *et al.*, Detection of dusty plasma near the e-ring of Saturn. *Planet. Space Sci.* **57**, 1795–1806 (2009).
7. P. K. Shukla, *Dust Plasma Interaction in Space* (Nova Publishers, 2002).
8. U. Kortshagen, Nonthermal plasma synthesis of semiconductor nanocrystals. *J. Phys. D Appl. Phys.* **42**, 113001 (2009).
9. R. L. Merlino, J. A. Goree, Dusty plasmas in the laboratory, industry, and space. *Phys. Today* **57**, 32–38 (2004).
10. J. Beckers, T. van de Ven, R. van der Horst, D. Astakhov, V. Banine, EUV-induced plasma: A peculiar phenomenon of a modern lithographic technology. *Appl. Sci.* **9**, 2827 (2019).
11. J. Winter, Dust: A new challenge in nuclear fusion research? *Phys. Plasmas* **7**, 3862–3866 (2000).
12. V. Tsytovich *et al.*, From plasma crystals and helical structures towards inorganic living matter. *New J. Phys.* **9**, 263 (2007).
13. L. S. Matthews *et al.*, Dust charging in dynamic ion wakes. *Phys. Plasmas* **27**, 023703 (2020).
14. A. Melzer, H. Krüger, D. Maier, S. Schütt, Physics of magnetized dusty plasmas. *Rev. Mod. Plasma Phys.* **5**, 11 (2021).
15. E. Thomas, R. Merlino, M. Rosenberg, Magnetized dusty plasmas: The next frontier for complex plasma research. *Plasma Phys. Control. Fusion* **54**, 124034 (2012).
16. A. Melzer, J. Goree, "Fundamentals of dusty plasmas" in *Low Temperature Plasmas Fundamentals, Technologies, and Techniques*, R. Hippler, H. Kersten, M. Schmidt, K. H. Schoenbach, Eds. (Wiley-VCH, ed. 2, 2008), vol. 1, pp. 157–206.
17. A. Melzer, H. Krueger, S. Schuett, M. Mulsow, Finite dust clusters under strong magnetic fields. *Phys. Plasmas* **26**, 093702 (2019).
18. V. Nikolaev, A. Timofeev, Nonhomogeneity of phase state in a dusty plasma monolayer with nonreciprocal particle interactions. *Phys. Plasmas* **28**, 033704 (2021).
19. D. A. Kolotinskii, V. S. Nikolaev, A. V. Timofeev, Effect of structural inhomogeneity and nonreciprocal effects in the interaction of macroparticles on the dynamic properties of a dusty plasma monolayer. *JETP Lett.* **113**, 510–517 (2021).
20. O. Vaulina, I. Lisina, E. Lisin, Energy exchange in systems of particles with nonreciprocal interaction. *J. Exp. Theor. Phys.* **121**, 717–726 (2015).
21. A. V. Ivlev *et al.*, Statistical mechanics where Newton's third law is broken. *Phys. Rev. X* **5**, 011035 (2015).
22. Z. Ding, K. Qiao, J. Kong, L. S. Matthews, T. W. Hyde, Nonlinear response of vertical paired structure in complex plasma. *Plasma Phys. Control. Fusion* **61**, 055004 (2019).
23. A. K. Mukhopadhyay, J. Goree, Two-particle distribution and correlation function for a 1D dusty plasma experiment. *Phys. Rev. Lett.* **109**, 165003 (2012).
24. Z. Ding, L. S. Matthews, T. W. Hyde, A machine learning based Bayesian optimization solution to non-linear responses in dusty plasmas. *Mach. Learn. Sci. Technol.* **2**, 035017 (2021).

25. W. Yu, J. Cho, J. C. Burton, Extracting forces from noisy dynamics in dusty plasmas. *Phys. Rev. E* **106**, 035303 (2022).

26. S. Nunomura, J. Goree, S. Hu, X. Wang, A. Bhattacharjee, Dispersion relations of longitudinal and transverse waves in two-dimensional screened coulomb crystals. *Phys. Rev. E* **65**, 066402 (2002).

27. L. Couëdel et al., First direct measurement of optical phonons in 2D plasma crystals. *Phys. Rev. Lett.* **103**, 215001 (2009).

28. L. Couëdel et al., Direct observation of mode-coupling instability in two-dimensional plasma crystals. *Phys. Rev. Lett.* **104**, 195001 (2010).

29. S. Zhdanov, A. Ivlev, G. Morfill, Mode-coupling instability of two-dimensional plasma crystals. *Phys. Plasmas* **16**, 083706 (2009).

30. U. Konopka, G. Morfill, L. Ratke, Measurement of the interaction potential of microspheres in the sheath of a RF discharge. *Phys. Rev. Lett.* **84**, 891 (2000).

31. G. Gogia, J. C. Burton, Emergent bistability and switching in a nonequilibrium crystal. *Phys. Rev. Lett.* **119**, 178004 (2017).

32. F. Greiner et al., Diagnostics and characterization of nanodust and nanodusty plasmas. *Eur. Phys. J. D* **72**, 1–12 (2018).

33. M. Lampe, G. Joyce, G. Ganguli, V. Gavrishchaka, Interactions between dust grains in a dusty plasma. *Phys. Plasmas* **7**, 3851–3861 (2000).

34. R. Gopalakrishnan, C. J. Hogan Jr., Coulomb-influenced collisions in aerosols and dusty plasmas. *Phys. Rev. E* **85**, 026410 (2012).

35. A. Ignatov, Interaction of grains in dusty plasmas. *J Phys. IV* **7**, C4–215 (1997).

36. B. J. Fulton, E. A. Petigura, S. Blunt, E. Sinukoff, Radvel: The radial velocity modeling toolkit. *Publ. Astron. Soc. Pac.* **130**, 044504 (2018).

37. M. Mayor, D. Queloz, A Jupiter-mass companion to a solar-type star. *nature* **378**, 355–359 (1995).

38. J. Pineda et al., Geometric deep learning reveals the spatiotemporal features of microscopic motion. *Nat. Mach. Intell.* **5**, 71–82 (2023).

39. D. B. Brückner et al., Learning the dynamics of cell-cell interactions in confined cell migration. *Proc. Natl. Acad. Sci. U.S.A.* **118**, e2016602118 (2021).

40. J. Toner, Y. Tu, Flocks, herds, and schools: A quantitative theory of flocking. *Phys. Rev. E* **58**, 4828 (1998).

41. V. Bapst et al., Unveiling the predictive power of static structure in glassy systems. *Nat. Phys.* **16**, 448–454 (2020).

42. J. Colen et al., Machine learning active-nematic hydrodynamics. *Proc. Natl. Acad. Sci. U.S.A.* **118**, e2016708118 (2021).

43. I. Tah, S. A. Ridout, A. J. Liu, Fragility in glassy liquids: A structural approach based on machine learning. *J. Chem. Phys.* **157**, 124501 (2022).

44. B. C. Daniels, W. S. Ryu, I. Nemenman, Automated, predictive, and interpretable inference of *Caenorhabditis elegans* escape dynamics. *Proc. Natl. Acad. Sci. U.S.A.* **116**, 7226–7231 (2019).

45. D. M. Anstine, O. Isayev, Machine learning interatomic potentials and long-range physics. *J. Phys. Chem. A* **127**, 2417–2431 (2023).

46. K. Champion, B. Lusch, J. N. Kutz, S. L. Brunton, Data-driven discovery of coordinates and governing equations. *Proc. Natl. Acad. Sci. U.S.A.* **116**, 22445–22451 (2019).

47. S. L. Brunton, J. L. Proctor, J. N. Kutz, Discovering governing equations from data by sparse identification of nonlinear dynamical systems. *Proc. Natl. Acad. Sci. U.S.A.* **113**, 3932–3937 (2016).

48. S. H. Rudy, S. L. Brunton, J. L. Proctor, J. N. Kutz, Data-driven discovery of partial differential equations. *Sci. Adv.* **3**, e1602614 (2017).

49. D. B. Brückner, P. Ronceray, C. P. Broedersz, Inferring the dynamics of underdamped stochastic systems. *Phys. Rev. Lett.* **125**, 058103 (2020).

50. P. Lemos, N. Jeffrey, M. Cranmer, S. Ho, P. Battaglia, Rediscovering orbital mechanics with machine learning. *Mach. Learn. Sci. Technol.* **4**, 045002 (2023).

51. C. Pandarinath et al., Inferring single-trial neural population dynamics using sequential auto-encoders. *Nat. Methods* **15**, 805–815 (2018).

52. B. C. Daniels, I. Nemenman, Automated adaptive inference of phenomenological dynamical models. *Nat. Commun.* **6**, 8133 (2015).

53. B. Chen et al., Automated discovery of fundamental variables hidden in experimental data. *Nat. Comput. Sci.* **2**, 433–442 (2022).

54. R. Supekar et al., Learning hydrodynamic equations for active matter from particle simulations and experiments. *Proc. Natl. Acad. Sci. U.S.A.* **120**, e2206994120 (2023).

55. M. Raissi, A. Yazdani, G. E. Karniadakis, Hidden fluid mechanics: Learning velocity and pressure fields from flow visualizations. *Science* **367**, 1026–1030 (2020).

56. M. Ruiz-Garcia et al., Discovering dynamic laws from observations: The case of self-propelled, interacting colloids. *Phys. Rev. E* **109**, 064611 (2024).

57. F. Battiston et al., The physics of higher-order interactions in complex systems. *Nat. Phys.* **17**, 1093–1098 (2021).

58. G. Carleo et al., Machine learning and the physical sciences. *Rev. Mod. Phys.* **91**, 045002 (2019).

59. G. E. Karniadakis et al., Physics-informed machine learning. *Nat. Rev. Phys.* **3**, 422–440 (2021).

60. F. Cichos, K. Gustavsson, B. Mehlig, G. Volpe, Machine learning for active matter. *Nat. Mach. Intell.* **2**, 94–103 (2020).

61. M. J. Falk, V. Alizadehyazdi, H. Jaeger, A. Murugan, Learning to control active matter. *Phys. Rev. Res.* **3**, 033291 (2021).

62. Z. Han, D. S. Kammer, O. Fink, Learning physics-consistent particle interactions. *PNAS Nexus* **1**, pgac264 (2022).

63. S. Greydanus, M. Dzamba, J. Yosinski, Hamiltonian neural networks. *Adv. Neural Inf. Process. Syst.* **32**, 15379–15389 (2019).

64. A. Sanchez-Gonzalez, V. Bapst, K. Cranmer, P. Battaglia, Hamiltonian graph networks with ode integrators. arXiv [Preprint] (2019). http://arxiv.org/abs/1909.12790 (Accessed 9 July 2025).

65. M. Lutter, C. Ritter, J. Peters, Deep lagrangian networks: Using physics as model prior for deep learning. arXiv [Preprint] (2019). http://arxiv.org/abs/1907.04490 (Accessed 9 July 2025).

66. J. Wang et al., Machine learning of coarse-grained molecular dynamics force fields. *ACS Cent. Sci.* **5**, 755–767 (2019).

67. M. Finzi, K. A. Wang, A. G. Wilson, Simplifying Hamiltonian and Lagrangian neural networks via explicit constraints. *Adv. Neural Inf. Process. Syst.* **33**, 13880–13889 (2020).

68. W. Huang et al., Equivariant graph mechanics networks with constraints. arXiv [Preprint] (2022). http://arxiv.org/abs/2203.06442 (Accessed 9 July 2025).

69. P. W. Battaglia et al., Relational inductive biases, deep learning, and graph networks. arXiv [Preprint] (2018). http://arxiv.org/abs/1806.01261 (Accessed 9 July 2025).

70. W. Yu, J. C. Burton, 3D tracking of particles in a dusty plasma by laser sheet tomography. *Phys. Plasmas* **30**, 063701 (2023).

71. O. Ishihara, S. V. Vladimirov, Wake potential of a dust grain in a plasma with ion flow. *Phys. Plasmas* **4**, 69–74 (1997).

72. P. Ludwig, W. J. Miloch, H. Kählert, M. Bonitz, On the wake structure in streaming complex plasmas. *New J. Phys.* **14**, 053016 (2012).

73. J. Goree, Charging of particles in a plasma. *Plasma Sour. Sci. Technol.* **3**, 400 (1994).

74. J. M. Harper, G. Gogia, B. Wu, Z. Laseter, J. C. Burton, Origin of large-amplitude oscillations of dust particles in a plasma sheath. *Phys. Rev. Res.* **2**, 033500 (2020).

75. T. Nitter, Levitation of dust in RF and DC glow discharges. *Plasma Sour. Sci. Technol.* **5**, 93 (1996).

76. P. S. Epstein, On the resistance experienced by spheres in their motion through gases. *Phys. Rev.* **23**, 710 (1924).

77. D. R. Gurevich, P. A. Reinbold, R. O. Grigoriev, Robust and optimal sparse regression for nonlinear PDE models. *Chaos Interdiscip. J. Nonlinear Sci.* **29**, 103113 (2019).

78. M. Cranmer et al., Discovering symbolic models from deep learning with inductive biases. *Adv. Neural Inf. Process. Syst.* **33**, 17429–17442 (2020).

79. S. V. Vladimirov, M. Nambu, Attraction of charged particulates in plasmas with finite flows. *Phys. Rev. E* **52**, R2172 (1995).

80. N. P. Kryuchkov, L. A. Mistryukova, A. V. Sapelkin, S. O. Yurchenko, Strange attractors induced by melting in systems with nonreciprocal effective interactions. *Phys. Rev. E* **101**, 063205 (2020).

81. D. Bohm, E. P. Gross, Effects of plasma boundaries in plasma oscillations. *Phys. Rev.* **79**, 992 (1950).

82. A. Douglass, V. Land, L. Matthews, T. Hyde, Dust particle charge in plasma with ion flow and electron depletion near plasma boundaries. *Phys. Plasmas* **18**, 083706 (2011).

83. A. Douglass, V. Land, K. Qiao, L. Matthews, T. Hyde, Determination of the levitation limits of dust particles within the sheath in complex plasma experiments. *Phys. Plasmas* **19**, 013707 (2012).

84. U. Konopka, L. Ratke, H. Thomas, Central collisions of charged dust particles in a plasma. *Phys. Rev. Lett.* **79**, 1269 (1997).

85. J. Carstensen, F. Greiner, A. Piel, Determination of dust grain charge and screening lengths in the plasma sheath by means of a controlled cluster rotation. *Phys. Plasmas* **17**, 083703 (2010).

86. P. K. Shukla, B. Eliasson, Colloquium: Fundamentals of dust-plasma interactions. *Rev. Mod. Phys.* **81**, 25 (2009).

87. P. K. Shukla, A. Mamun, *Introduction to Dusty Plasma Physics* (CRC Press, 2015).

88. A. Ignatov, Basics of dusty plasma. *Plasma Phys. Rep.* **31**, 46–56 (2005).

89. F. Galli, U. R. Kortshagen, Charging, coagulation, and heating model of nanoparticles in a low-pressure plasma accounting for ion-neutral collisions. *IEEE Trans. Plasma Sci.* **38**, 803–809 (2010).

90. M. Gatti, U. Kortshagen, Analytical model of particle charging in plasmas over a wide range of collisionality. *Phys. Rev. E* **78**, 046402 (2008).

91. D. B. Allan, T. Caswell, N. C. Keim, C. M. van der Wel, R. W. Verweij, soft-matter/trackpy: v0.6.4 (v0.6.4). Zenodo. https://doi.org/10.5281/zenodo.12708864. Accessed 10 July 2025.

92. W. Yu, wyu54/many-body-force-infer: Dusty plasma force infer (ML). Zenodo. https://doi.org/10.5281/zenodo.15866620. Accessed 10 July 2025.